Residual stresses and microstructure in fine grained cemented carbides doped with Cr and Ti

International Journal of Refractory Metals and Hard Materials 128 (2025) 107005

Contents lists available at ScienceDirect

International Journal of Refractory Metals and Hard Materials

journal homepage: www.elsevier.com/locate/IJRMHM

Residual stresses and microstructure in fine grained cemented carbides doped with Cr and Ti

J. Weidow [a,*], A.B. Yildiz [b], G. Olsson [a], V. Lilja [a], S. Sten [c], I. Borgh [c], P. Hedström [e], M. Kritikos [d], F. Lindberg [d], E. Coronel [d], J. Kelleher [f], D. Mayweg [a], M. Thuvander [a], S. Norgren [c,d,g]

[a] Department of Physics, Chalmers University of Technology, 412 96 Göteborg, Sweden
[b] Scatterin AB, Drottning Kristinas väg 53, 114 28 Stockholm, Sweden
[c] Sandvik Mining and Rock Solutions, R&D Rock Tools, 126 80 Stockholm, Sweden
[d] AB Sandvik Coromant, R&D Materials and Processes, 126 80 Stockholm, Sweden
[e] Department of Materials Science and Engineering, KTH Royal Institute of Technology, 100 44 Stockholm, Sweden
[f] ISIS Facility, Harwell Campus, Didcot OX11 0QX, UK
[g] Division of Production and Materials Engineering, Lund University, 221 00 Lund, Sweden

ARTICLE INFO

Keywords:
Residual stress
WC-Co
Hard metal
Fine grained

ABSTRACT

Three fine grained WC-10 vol% Co cemented carbide materials were produced. One with 1 w% Cr addition, one with 0.025 w% Ti addition and one with both additions of 1 w% Cr and 0.025 w% Ti. It was found that doping of both Cr and Ti is advantageous for grain growth inhibition over just Cr- or Ti-doping. The impact of Cr and Ti as grain growth inhibitors on the residual stress state after sintering was investigated. The stress state in the centre of the composite, in WC and Co phase, was quantified by neutron diffraction. The addition of Ti and Cr significantly affects the residual stresses in WC. Notably, the co-doped material exhibits the lowest WC residual stresses despite rather similar WC average grain sizes and binder phase volume fractions compared to the Cr-doped material. This suggests that factors beyond grain size and Co-rich binder volume fraction can play a crucial role in residual stress development. Alterations in binder composition and resulting changes in binder stacking fault energy, thermal expansion coefficient and interface structures as well as changes of the solidification temperature are proposed to also effect the WC residual stresses, and further work is suggested to detail the underlying mechanisms.

1. Introduction

Cemented carbides are important materials in metal cutting and rock drilling applications. Their composite structure, combining the hardness of a carbide phase (conventionally WC) with the toughness of a metallic binder phase (conventionally Co-rich) provides excellent mechanical properties for the harsh conditions imposed during service in the mentioned applications. The mechanical properties of the final composite depend on the WC grain size according to the Hall-Petch relation and thus it is key to control grain growth during the powder metallurgical manufacturing of cemented carbides. The final step of the manufacturing is liquid phase sintering which generally takes place at temperatures around 1400 °C. During this step, the liquid Co-rich binder facilitates the densification of the composite. Also, the WC grains are particularly prone to coarsening at this stage. To inhibit grain coarsening it is common to add Cr_3C_2 and/or TiC powders during production of cemented carbides [1]. These additions change the interface properties between WC/WC grains and between WC and the binder phase and hinder the coarsening of the microstructure [2–6].

During the cooling after liquid phase sintering, residual stresses build up in the cemented carbide due to thermal expansion differences between the solidifying Co-rich binder phase and WC grains and phase transformation [7]. Previous studies have indicated that the contraction of the binder phase during cooling leads to high tensile residual stresses within the binder phase, which in turn induce compressive residual stresses in the WC skeleton. The residual stresses affect the behaviour of the material during service or subsequent processing, e.g. under external load, and affect strength, dimensional stability, and fatigue life of the

* Corresponding author.
E-mail address: jonathan.weidow@chalmers.se (J. Weidow).

https://doi.org/10.1016/j.ijrmhm.2024.107005
Received 10 October 2024; Received in revised form 2 December 2024; Accepted 2 December 2024
Available online 5 December 2024

material [8,9]. Although residual stresses can trigger premature component failure at low load levels, compressive residual stresses can also be beneficial and impede crack growth or change the crack growth direction. Control of beneficial residual stresses are particularly important for cemented carbide tools used in demanding applications where they can be exposed to temperatures in the order of 1000 °C and applied stresses up to about 2 GPa. A comprehensive understanding of residual stresses and their quantification are thus crucial for cemented carbide industry to accurately predict tool performance and achieve structural integrity during production and service. Previous work on residual stresses in WC-Co cemented carbides have focused on the impact of WC grain size and binder content [10]. The results have shown that the magnitude of residual stresses in WC increases with decreasing average WC grain size and increasing binder content. However, although Cr and Ti additions are widely used in metal cutting and rock drilling tools, their impact on residual stress formation is yet to be investigated.

In this work, the impact of Cr and Ti as grain growth inhibitors on the residual stress state in submicron WC grain size cemented carbide after sintering is investigated. The stress state in the WC and Co phase was quantified by neutron diffraction. The materials were produced from the same WC and Co raw materials and the aim of the study is to systematically evaluate the effect of additions of Cr and/or Ti on the microstructure and residual stresses.

2. Experimental and theoretical method

2.1. Material production

Three fine grained WC-10 vol% Co cemented carbide materials were produced. One with 1 w% Cr additions, one with 0.025 w% Ti additions and one with both addition of 1 w% Cr and 0.025 w% Ti.

The starting powder mixtures contained WC + Co + Cr_3C_2 and/or TiC. Raw materials used was WC (0.8 μm FSSS) from Wolfram Bergbau und Hütten AG, Co (1.4 μm FSSS), from Freeport, Cr_2C_3 (1.5 μm FSSS) and TiC (1.8 μm FSSS) from Treibacher Industrie AG. W and C was added to adjust the C level. In addition, 2 w% polyethylene glycol was added as pressing agent together with ethanol as milling liquid. The powders were ball milled for 25 h and then spray dried. Cylindrical green bodies were cold isostatically pressed and then gas pressure sintered at 1410 °C under 55 bar Ar pressure with a holding time of one hour followed by furnace cooling.

After sintering the materials were analysed using standard magnetic property measurements of coercivity and relative magnetic saturation. Furthermore, hardness was evaluated using Vickers hardness testing with a load of 20 kg. Coercivity was measured on three different samples and hardness using 5 indents on one sample. The error was calculated assuming a normal confidence interval of 95 %.

2.2. Thermodynamic calculations

Thermodynamic calculations were performed using Thermo-Calc software and database TCFE13 [11]. TCFE13 database is a steel database but contains assessments for relevant systems for cemented carbide calculations. In the calculations, some phases were removed, depending on the composition of the material. For the Cr- and co-doped systems M_3C_2, cementite (M_3C) and W_2C (HCP) were removed. It is known from experiments that M_7C_3 and graphite will form instead of M_3C_2 (where M = Ti,Cr,W) and cementite (M_3C, where M = W,Co) and hence these were removed. W_2C was removed since it has never experimentally been identified. For the Ti-doped system only cementite (M_3C) and HCP phases were removed, with the same arguments as above. The removal of M_3C_2 in this case though caused abnormal appearance of the phase diagram and it was therefore kept in the calculations. Isopleths for the three systems were evaluated. It was furthermore assumed that the mobility of atoms is sluggish below 1000 °C and that the binder composition freezes in at that temperature [12]. Therefore, phase stability and binder composition were calculated at 1000 °C. Moreover, the volumetric thermal expansion coefficient, β, was calculated at 1000 °C for the FCC Co- rich binder phase and for WC. For the Cr-doped system composition of the M_7C_3 was also calculated.

2.3. SEM imaging and electron backscatter diffraction (EBSD) analysis

The as-sintered materials were prepared according to standard materialographic preparation methods including cutting, grinding and mechanical polishing. Final mechanical polishing was conducted using 1 μm diamond particles. The material sections were imaged using a Jeol JSM-7800F scanning electron microscope in backscattered electron (BSE) imaging mode. The acceleration voltage used was 10 kV, and the working distance was 6 mm.

The specimens prepared for electron backscatter diffraction (EBSD) analysis were cut in 4 × 4 mm pieces with 250 μm thickness. After following the same preparation protocol as for the specimens for SEM imaging, these were subsequently polished for 2 h by Ar^+ ion sputtering in a Gatan precision ion polishing system Model 695 at 4.0 kV with a 2° incident angle. EBSD analyses were carried out in a TESCAN GAIA3 workstation equipped with an Oxford NordlysNano camera. The workstation was used at 20 kV, spot size 12.0 nm and working distance 9 mm. The software AZtecHKL and Tango were used for the analyses.

2.4. Atom probe tomography

The as-sintered material pieces were cut in rods with the cross-section 300 × 300 μm. The rods were thereafter electropolished by immersing the rod in a highly viscous lacquer (Lacomite). An electrolyte consisting of 5 % H_2SO_4 in ethanol was cooled to −30 °C. Electropolishing was performed at 29 V using a circular golden counter electrode thus creating a waist-shaped specimen where eventually the bottom half fell off. To further sharpen the specimen, a second electrolyte, 5 % H_2SO_4 in methanol, was prepared and cooled to −20 °C. Using a platinum foil counter electrode, between one and three 10 ms pulses of 20 V were applied. The pulse length was then gradually reduced to 2 ms, 1 ms and 0.5 ms with eight pulses applied per pulse length. A typical analysis of a cemented carbide sample with atom probe tomography (APT) is in the range of 10–100 nm, this means the nanostructure feature of interest, e.g. a phase boundary, needs to be located within 100 nm from the tip of the specimen. Moreover, as the field for field evaporation of WC is substantially larger than for the Co-rich binder phase, it is also necessary that the analysis starts with the binder phase. Therefore, final polishing of the APT specimens was conducted by Ga ion milling in a FEI Versa3D workstation.

A Cameca LEAP 6000 XR was used for the APT analyses. The analyses were performed in laser mode with the energy 30 pJ, frequency 200 kHz, detection rates 0.2–0.5 % and temperature 66 K. For the reconstructions, 37 V/nm was generally used as the field needed for field evaporation. In the case when calculating the thickness of the analysed WC/WC grain boundary, the field 58 V/nm was instead used.

2.5. Neutron diffraction

Time-of-flight (TOF) neutron diffraction experiments were performed on the Engin-X instrument at the ISIS Neutron and Muon Source in the UK, using a polychromatic neutron beam with wavelength range from 0.85 to 2.62 Å. Hour-glass shaped samples with center diameter of 6 mm were used, and 4 × 4 × 4 mm^3 gauge volume was defined in the center of the samples. By maintaining 45° angle between the incoming beam and the sample and using ±90° detector banks, TOF diffraction enables simultaneous acquisition of diffraction patterns with a wide range of interplanar lattice spacings from two orthogonal directions. For cylindrical samples, this allows for the simultaneous measurements of lattice strain in axial and radial (transverse) directions. The experimental setup is illustrated in Fig. 1.

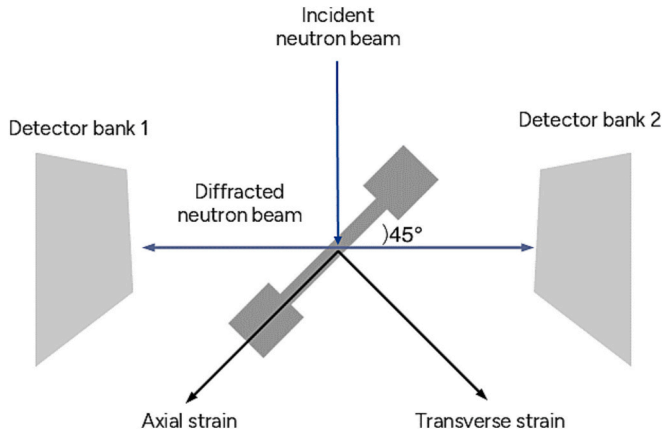

Fig. 1. Schematic of the TOF neutron diffraction residual stress measurement setup at Engin-X, ISIS. Schematic adapted from Heshmati et al. [13].

Parameters critical for defining instrumental broadening and accurate conversion of TOF to d-spacing were determined by measuring a CeO_2 reference powder on both detector banks.

To determine lattice parameters, peak broadening, crystallite size, and microstrain, the collected TOF diffraction patterns were analysed by Rietveld refinement method using Scatterin SaaS data analysis software [14]. The Rietveld refinement method simulates a powder diffraction pattern based on various intrinsic, e.g. lattice parameter and crystallite size, and extrinsic parameters such as instrument profile parameters. During the structural refinement, simulated pattern is least-squares fitted to the measured diffraction data to determine microstructural parameters [15,16]. The lattice parameters of WC were used for calculating WC lattice strain:

$$\varepsilon_a = \frac{a - a_0}{a_0} \tag{1}$$

and

$$\varepsilon_c = \frac{c - c_0}{c_0} \tag{2}$$

where a_0 and c_0 are the stress-free reference lattice parameters of WC [17]. The WC lattice strains were combined to define average strain ε in WC phase by [18]:

$$\varepsilon = \frac{2\varepsilon_a + \varepsilon_c}{3} \tag{3}$$

Since the Co-rich binder phase creates solute solution with C, W, and doping elements such as Cr and Ti, with a varying composition depending on the nominal composition, it is not possible to accurately determine the stress-free lattice parameter for Co-rich binder phase. We therefore limit the strain measurements to WC phase and employ two different methodologies to estimate residual strain and stress in binder phase, as further discussed in the Discussion section. By assuming cylindrically symmetric stress over the gauge volume, i.e. radial stresses are equal to hoop stresses in the center of a cylindrical sample, the residual stresses in axial σ_{axial} and transverse j directions can be calculated by:

$$\sigma_{axial} = \frac{1}{s_2/2}\left[\varepsilon_{axial} - \left(\frac{s_1}{s_2/2 + 3s_1}\right)(2\varepsilon_{transverse} + \varepsilon_{axial})\right] \tag{4}$$

$$\sigma_{transverse} = \frac{1}{s_2/2}\left[\varepsilon_{transverse} - \left(\frac{s_1}{s_2/2 + 3s_1}\right)(2\varepsilon_{axial} + \varepsilon_{transverse})\right] \tag{5}$$

where s_1 and $s_2/2$ are the diffraction elastic constants and equal to -3.539×10^{-5} MPa^{-1} and 1.8214×10^{-6} MPa [18]. $s_1 = -\nu/E$ and $s_2/2 = (1+\nu)/E$, where E the elastic modulus and ν is the Poisson's ratio.

3. Results

3.1. Material production

The three produced cemented carbide materials were analysed using standard characterization methods and the results are shown in Table 1. The measurement of the relative magnetic saturation shows equal values for the three materials, indicating that all three materials ended up at equal C contents and between the two limits of η phase and graphite, as intended. The co-doped material had the highest coercivity and the highest hardness, while the Ti-doped material shows the lowest coercivity and hardness. Hence, according to magnetic coercivity and Hall-Petch relation it is indicated that Ti-doped material has the largest WC grain size, whilst the co-doped material has the lowest WC grain size.

3.2. Thermodynamic calculations

From the isopleths in Fig. 2. for the three material systems, it is seen that the doping elements will affect both liquidus/solidus temperature as well as the stable phases for the cemented carbide. When Cr is added, M_7C_3 becomes stable at higher C contents and when Ti is added a second FCC phase, the MC-carbide ("γ" phase) will form, where M = Ti,Cr,W.

The range in C content for the desired region WC-Co-(M_7C_3/ γ) can be calculated by evaluating the C content at the limit to the WC-Co-η region as well as the limit to the WC-Co-Graphite-(M_7C_3/ γ) region at 1000 °C. From Fig. 2. it is seen that Cr addition will widen the range in C. For these limits, η and graphite, the stable phases and their volume fraction together with Co-rich binder phase composition have been calculated by single point equilibrium calculations, given in Tables 2–5. It should be noticed that all three materials are within the desired region and should end up with compositions in between these end points.

The W and C solubility in the binder differs depending on where in the C range the composition is evaluated. As expected, a higher W solubility and lower C solubility can be seen at the η phase limit compared with the graphite limit and vice versa. The higher W solubility at η phase limit is the major factor to the increase in volume of the Co-rich binder phase (FCC).

The volume fraction of Co-rich binder phase is higher for all materials at the limit to the η phase compared to the graphite limit due to the difference in W solubility. The difference in volume fraction is further related to the formation/or higher volume fractions of the carbide formed, γ((Ti,Cr,W)C and (Ti,W)C) and M_7C_3 when more C is available.

At the graphite limit, Cr and Ti solubility in the Co-rich binder is unchanged when adding a second doping element, i.e. for the co-doped system. Further, a higher solubility of W and C in the Co-rich binder can be seen when Cr is added.

At the η phase limit, equal solubility of W in the Co-rich binder can be seen for all three materials. Solubility of C in the Co-rich binder is higher when Cr is added. The Ti solubility in the Co-rich binder differs depending on if Cr is present or not.

The composition of the M_7C_3 carbide was calculated at the graphite limit at 1000 °C for the Cr-doped system. The calculations showed a composition of 46 at.% Cr, 22 at.% Co, 1.2 at.% W and 30 at.%C.

Results from the calculations of the volumetric thermal expansion

Table 1
As-sintered material properties.

Cr additions (w%)	Ti additions (w%)	Coercivity (kA/m)	Relative magnetic saturation	Hardness HV20 (GPa)
1	0	20.20 ± 0.01	0.83	16.58 ± 0.07
0	0.025	16.38 ± 0.02	0.82	14.61 ± 0.08
1	0.025	21.57 ± 0.03	0.85	17.10 ± 0.07

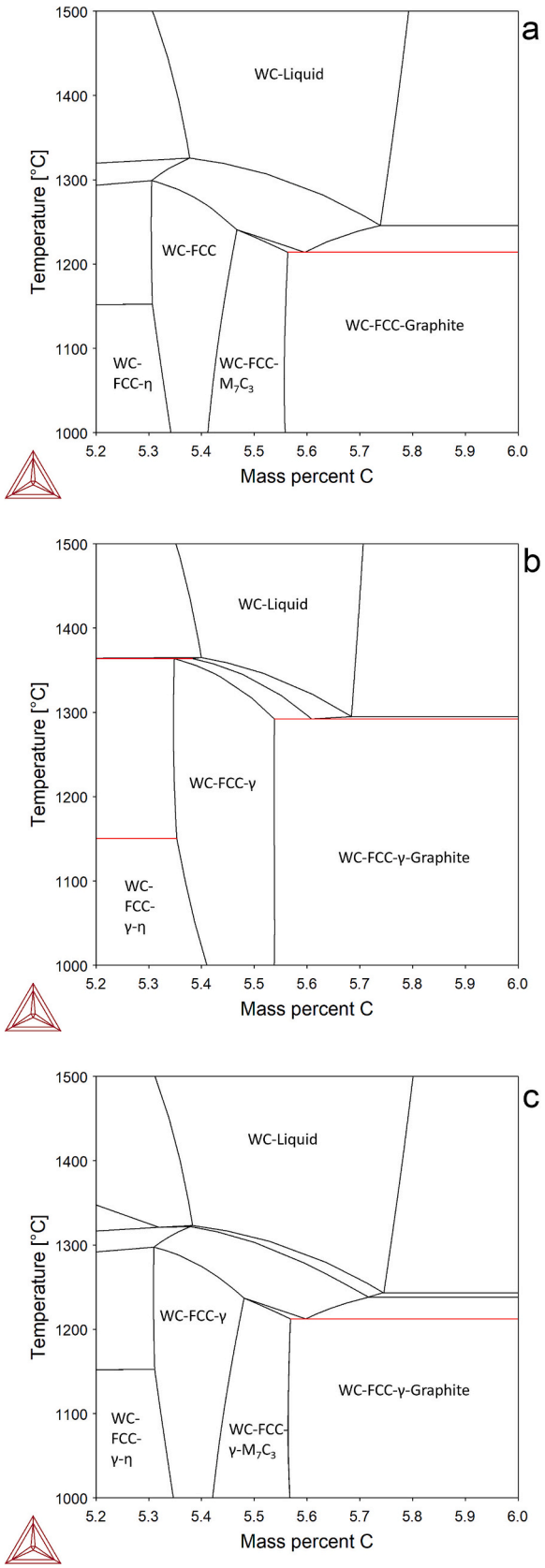

Fig. 2. Isopleths for the three material systems calculated using Themo Calc software and the TCFE13 database [11]. In a) Cr doped system, in b) Ti doped system and in C) Co-doped systems.

Table 2
Stable phases at 1000 °C at the limit to η phase.

Cr additions (w%)	Ti additions (w%)	Co FCC (vol fr)	(Ti,Cr, W)C (vol fr)	WC (vol fr)	M_7C_3 (vol fr)	(Ti,W)C (vol fr)
1	0	0.21		0.79		
0	0.025	0.19		0.81		0.0010
1	0.025	0.21	0.0013	0.79		

Table 3
Stable phases at 1000 °C at the limit to graphite.

Cr additions (w%)	Ti additions (w%)	Co FCC (vol fr)	(Ti,Cr, W)C (vol fr)	WC (vol fr)	M_7C_3 (vol fr)	(Ti,W)C (vol fr)
1	0	0.18		0.80	0.019	
0	0.025	0.17		0.83		0.0012
1	0.025	0.18	0.0031	0.80	0.016	

Table 4
Co-rich binder (FCC) composition at 1000 °C at the η phase limit.

Cr additions (w%)	Ti additions (w%)	C (at. %)	Co (at.%)	Ti (at. %)	Cr (at. %)	W (at. %)
1	0	0.58	84		9.5	5.7
0	0.025	0.30	94	0.060		5.8
1	0.025	0.58	84	0.020	9.5	5.7

Table 5
Co-rich binder (FCC) composition at 1000 °C at the graphite limit.

Cr additions (w%)	Ti additions (w%)	C (at. %)	Co (at. %)	Ti (at. %)	Cr (at. %)	W (at. %)
1	0	2.3	92		4.9	0.92
0	0.025	1.2	98	0.01		0.45
1	0.025	2.3	92	0.01	4.9	0.92

coefficient, β, can be seen in Table 6. According to literature, β for pure Co at 1000 °C is 0.000046 K^{-1} [19]. If the calculated value is compared with the reference value one can see that they are in the same order of magnitude. Comparing β for the FCC phase between the three material systems one can see that it is higher for all three systems at the η phase limit compared to the graphite limit and that the differences are predicted to be large. In the calculations, WC is modelled as a stochiometric phase independent of system composition and hence calculations of β for WC will give the same value of all three systems and both limits as seen in Table 6. Comparing β between the two phases, FCC and WC, one can see that β for FCC is calculated to be more than double or three times higher than for WC. The large differences seen for the FCC phase between the three systems and between FCC and WC may be a cause of the thermodynamic description of these systems.

Table 6
Calculated volumetric thermal expansion coefficient, β, for FCC at 1000 °C.

Cr additions (w%	Ti additions (w%	β for FCC at η phase limit (K^{-1})	β for WC at η phase limit (K^{-1})	β for FCC at graphite limit (K^{-1})	β for WC at graphite limit (K^{-1})
1	0	0.000056	0.000020	0.000024	0.000020
0	0.02	0.000022	0.000020	0.000010	0.000020
1	0.02	0.000067	0.000020	0.000066	0.000020

3.3. SEM imaging and electron backscatter diffraction (EBSD) analysis

Backscattered overview images of the structure for the three materials can be seen in Fig. 3. It appears that the co-doped material has a slightly smaller WC grain size than the Cr-doped material but a much smaller WC grain size than the Ti-doped. For the Ti-doped material, there appears to exist larger elongated WC grains. No signs of η phase or graphite can be seen for any of the three materials.

The results from the EBSD analysis are shown in Table 7 confirming the co-doped material having the smallest WC grain size followed by the Cr-doped and the Ti-doped having the coarsest WC grains. The grain size measurements are here given as mean radii. The ± show the uncertainty for the mean grain sizes and is calculated for a 95 % confidence interval assuming a normal distribution.

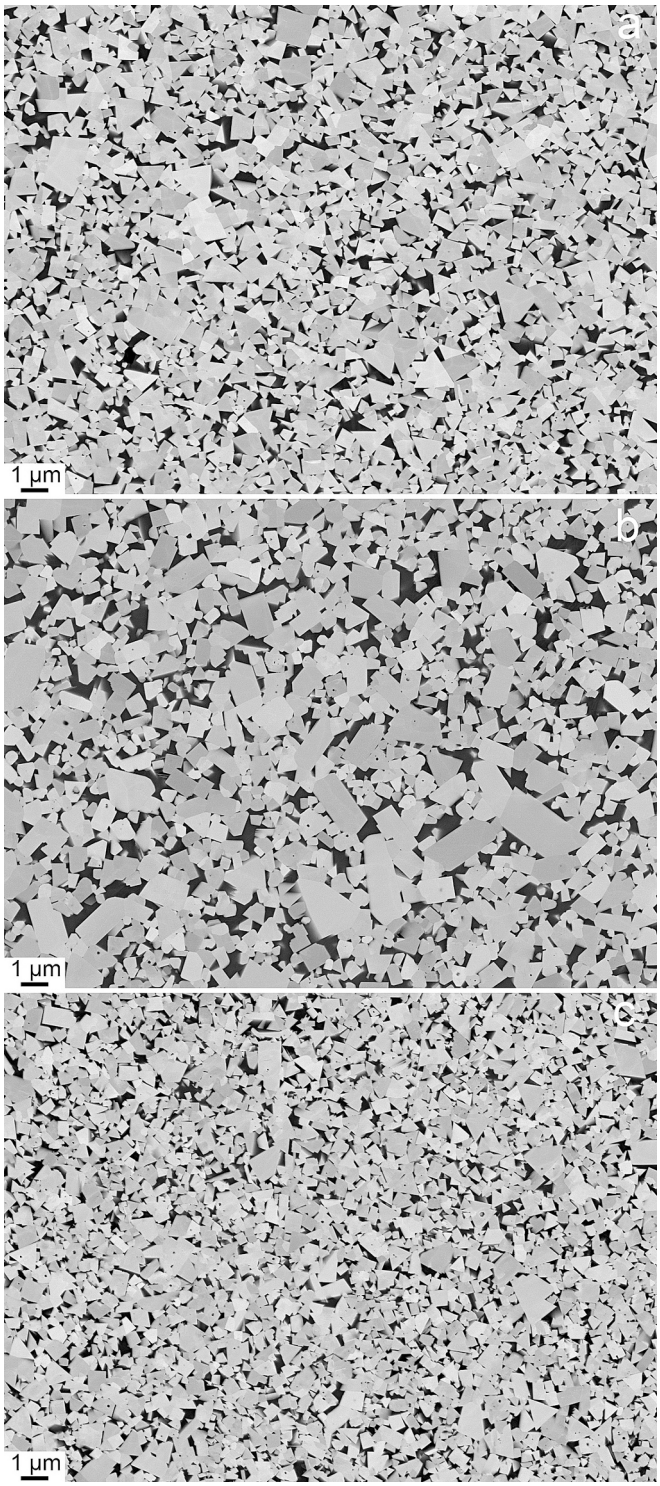

Fig. 3. SEM images of the as-sintered materials.

Table 7
EBSD analysis results for WC grains.

Cr additions (w%)	Ti additions (w%)	WC grain size (μm)	Std. Deviation (μm)	Grains investigated
1	0	0.418 ± 0.008	0.190	1921
0	0.025	0.487 ± 0.012	0.271	1877
1	0.025	0.377 ± 0.008	0.170	1662

3.4. Atom probe tomography

One specimen of each of the three materials was successfully analysed with APT. The compositions of the binder phase for the three materials are shown in Table 8. Cr has a large tendency to dissolve in the Co-rich binder phase but not Ti. The fraction of dissolved W in the binder phase is much higher for the material without any additions of Cr compared to the materials with additions of Cr.

The analysed phase boundary in the material with Cr addition revealed a Cr rich layer at the interface, see Figs. 4 and 5. This layer corresponds to 0.65 monolayer close packed Cr. In the interface region, a Cr rich particle was observed. An isosurface with the threshold 30 at. % Cr was created around the particle. The composition of the enclosed volume was, in at. %, C 30.8, Co 9.8, W 18.6 and Cr 40.8.

The analysis of the interface in the material with additions of both Cr and Ti showed no additional Cr or Ti at the interface.

The analysis of the interface in the material with additions of Ti showed no additional Ti at the interface. However, a WC/WC grain boundary was revealed directly after the phase boundary, see Fig. 6. The analysis of the grain boundary showed segregation of both Co and Ti. The amount of Co corresponded to 1.8 monolayers and the amount of Ti to 1.5 monolayers. With a view perpendicular to the interface, a striped pattern in the Co signal can be observed, see Fig. 7.

3.5. Neutron diffraction

Fig. 8 shows a representative TOF diffraction pattern from studied cemented carbide samples revealing multiple WC diffraction peaks and (111), (200), and (311) reflections of Co-rich binder phase.

Table 9 shows the lattice parameters of WC and Co-rich binder phases in axial and transverse directions, determined by Rietveld refinement, for the three materials. The lattice parameters of WC phase are smaller than the reference values in all samples, indicating compressive residual stresses. Due to the composite nature of the cemented carbides, the stress balance induces tensile residual stresses in the Co-rich binder phase. However, the accurate interpretation of the binder lattice parameters is challenging due to the lack of precise stress-free reference lattice parameters.

Fig. 9 shows the residual stresses in axial and transverse directions

Table 8
Composition of the binder phase as measured with atom probe tomography.

Cr additions (w%)	Ti additions (w%)	Co (at. %)	W (at. %)	C (at. %)	Cr (at. %)	Ti (at. %)
1	0	90.36 ± 0.10	1.29 ± 0.01	0.22 ± 0.01	8.13 ± 0.03	
0	0.025	95.13 ± 0.07	4.76 ± 0.02	0.00 ± 0.01		0.03 ± 0.01
1	0.025	89.38 ± 0.23	1.47 ± 0.03	0.64 ± 0.02	8.47 ± 0.07	0.04 ± 0.01

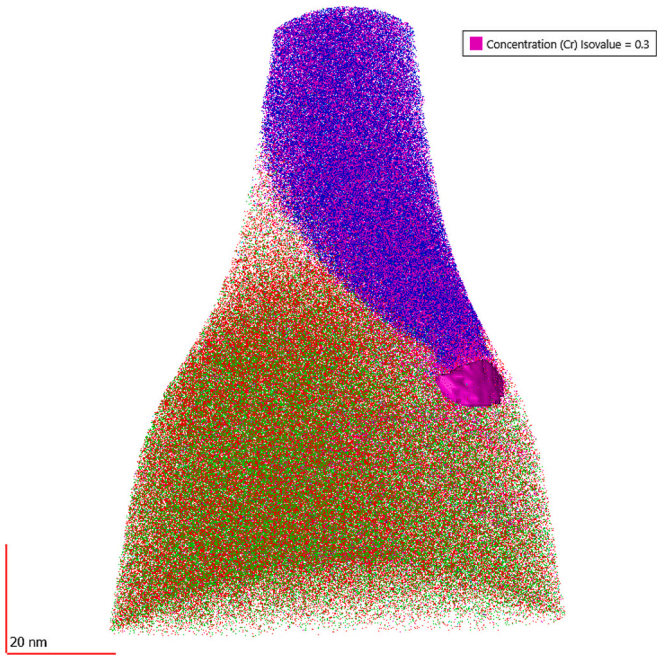

Fig. 4. Reconstruction of an atom probe tomography analysis of the WC-Co material with Cr additions. Each atom is represented with a dot, blue = Co, green = W, red = C, pink = Cr. In addition, an isosurface is enclosing a Cr-rich region. (For interpretation of the references to colour in this figure legend, the reader is referred to the web version of this article.)

for the three materials. The results reveal that the addition of minor amounts of Ti, i.e. 0.025 wt%, in co-doped material remarkably reduces the residual stresses compared to Cr-doped system. The Ti-doped and the co-doped materials, on the other hand, exhibited relatively similar stress levels which were lower than Cr-doped material. The results suggest that the Ti addition has a predominant role in residual stress reduction. Furthermore, whilst higher compressive residual stresses, i.e. more negative values, are observed in the transverse direction for the Cr- and Ti-doped materials, axial and transverse residual stresses have similar values in the co-doped material.

Fig. 10 show the microstrain (intragranular strain) and crystallite size of WC phase in the three materials, respectively. It is revealed that the microstrain and crystallite size values vary significantly with the minor changes in the composition. As seen in Fig. 10a, the highest microstrain values in WC are observed in the Cr-doped material. The addition of Ti reduces the microstrain in WC. The Ti-doped material has the lowest microstrain at about 700 $\times$ 10^{-6} in axial and 550 $\times$ 10^{-6} in transverse direction, compared to 925 $\times$ 10^{-6} (axial) and 975 $\times$ 10^{-6} (transverse) for the Cr-doped material. As expected from the average WC grain size values determined by EBSD, Fig. 10b reveals that Ti-doped material has the highest WC crystallite size followed by Cr-doped and co-doped materials, respectively. For all materials, higher crystallite size values are observed in the transverse direction.

4. Discussion

4.1. Microstructural evolution

The results in this study show that the most fine-grained material is

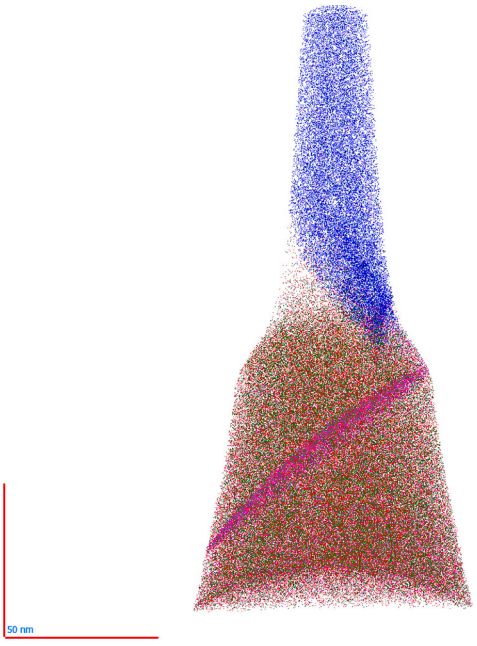

Fig. 6. Reconstruction of an atom probe tomography analysis of the WC-Co material with Ti additions. Each atom is represented with a dot, blue = Co, green = W, red = C, pink = Ti. (For interpretation of the references to colour in this figure legend, the reader is referred to the web version of this article.)

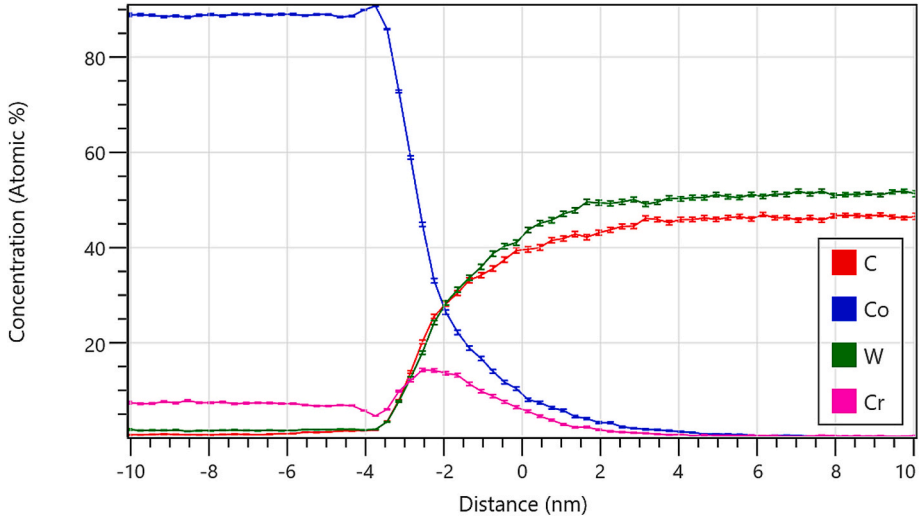

Fig. 5. Proxigram of a binder/WC interface in the WC-Co material with Cr additions.

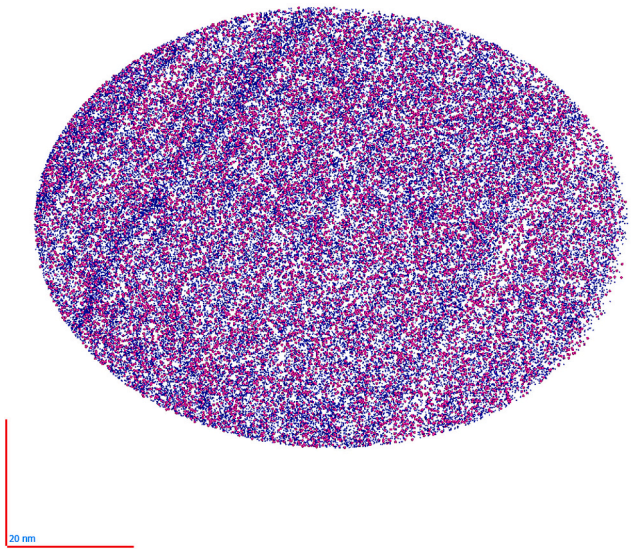

Fig. 7. Reconstruction of an atom probe tomography analysis of a WC/WC interface in the WC-Co material with Ti additions. Each atom is represented with a dot, blue = Co, pink = Ti. (For interpretation of the references to colour in this figure legend, the reader is referred to the web version of this article.)

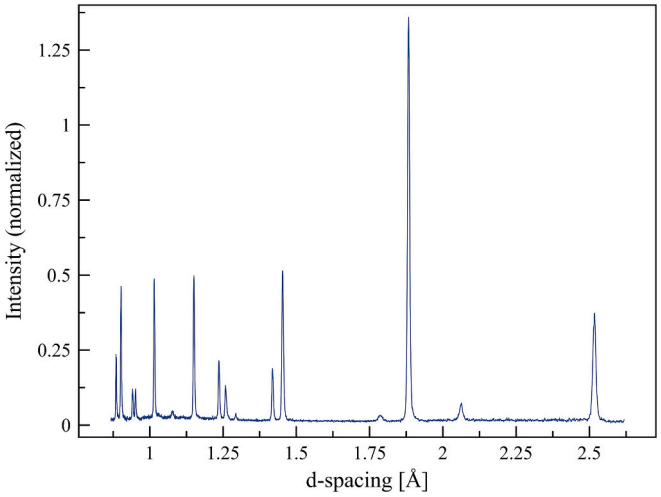

Fig. 8. Typical TOF neutron diffraction pattern of WC-Co cemented carbides studied in the present work.

the co-doped material with both Cr and Ti. It has the smallest WC grain size, the highest hardness and the highest coercivity. The material with the largest WC grain size, the Ti-doped, is the softest of the three materials and show the lowest coercivity. It was expected that 1 w% Cr additions would have a larger grain growth inhibiting effect than 0.025 w% Ti additions [1].

The thermodynamic calculations cannot verify the solubility differences in the Co-rich binder depending on doping as observed by APT. The calculations show the same trend but opposite. One reason is that the thermodynamic evaluation for these systems needs to be re-assessed. Another possibility is that the proximity to the phase boundary make the chemistry different from that in the bulk.

The proxigram of the WC/binder interface suggests that the WC phase is understoichiometric. However, this is rather a sign of difficulty of analysing carbides where a fraction of the C atoms is missed in the detection due to clustering in the field evaporation process [21].

Segregation of Cr has been observed at the WC/binder interfaces several times [2,5]. Also, segregation of Ti to WC/binder interfaces has been reported [6]. The presence of atoms from the dopants are believed to hinder the WC grain growth. Analysis of interfaces with APT is difficult, thus the statistics in terms of number of analysed interfaces is poor. Also, it is not possible to know afterwards which orientation relationship that was present for the interface as the specimen has been consumed.

This study revealed the possible presence of a 5–10 nm sized Cr-rich particle at the WC/binder interface. Based on the composition it is assumed to be a M_7C_3 phase. Comparing with the phase diagrams this is also the stable phase. If the calculated composition of the M_7C_3 phase at the graphite limit and 1000 °C is compared with the analysed composition with APT the agreement is rather good. The largest differences can

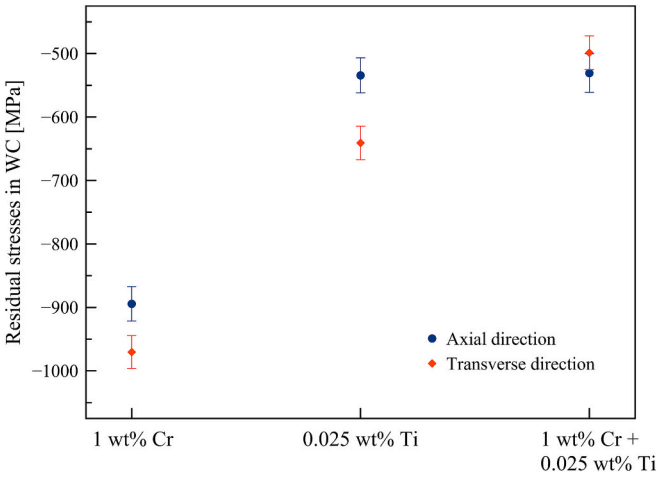

Fig. 9. Residual stresses in WC in axial and transverse directions.

Table 9
Lattice parameters of WC and Co-rich binder phases in axial and transverse directions determined by Rietveld refinement. For reference at room temperature: (i) stoichiometric hexagonal WC lattice parameters are a = b = 2.9059 Å and c = 2.8377 Å [17], and (ii) pure face-centered cubic Co lattice parameter is a = b = c = 3.5447 Å [20].

		WC lattice parameter (Å)				Binder lattice par. (Å)	
		a = b		c		a = b = c	
Cr additions (w %)	Ti additions (w %)	Axial	Transverse	Axial	Transverse	Axial	Transverse
1	0	2.9046 ± 1.168 × 10^{-4}	2.9037 ± 1.061 × 10^{-4}	2.8354 ± 9.45 × 10^{-5}	2.8349 ± 8.705 × 10^{-5}	3.5684 ± 1.083 × 10^{-3}	3.5676 ± 8.13 × 10^{-4}
0	0.025	2.9053 ± 1.205 × 10^{-4}	2.9041 ± 1.077 × 10^{-4}	2.8367 ± 9.75 × 10^{-5}	2.8359 ± 8.961 × 10^{-5}	3.5728 ± 1.046 × 10^{-3}	3.5716 ± 8.27 × 10^{-4}
1	0.025	2.9048 ± 1.388 × 10^{-4}	2.9051 ± 9.74 × 10^{-5}	2.8360 ± 1.141 × 10^{-4}	2.8364 ± 8.217 × 10^{-5}	3.5705 ± 1.116 × 10^{-3}	3.5714 ± 6.31 × 10^{-4}

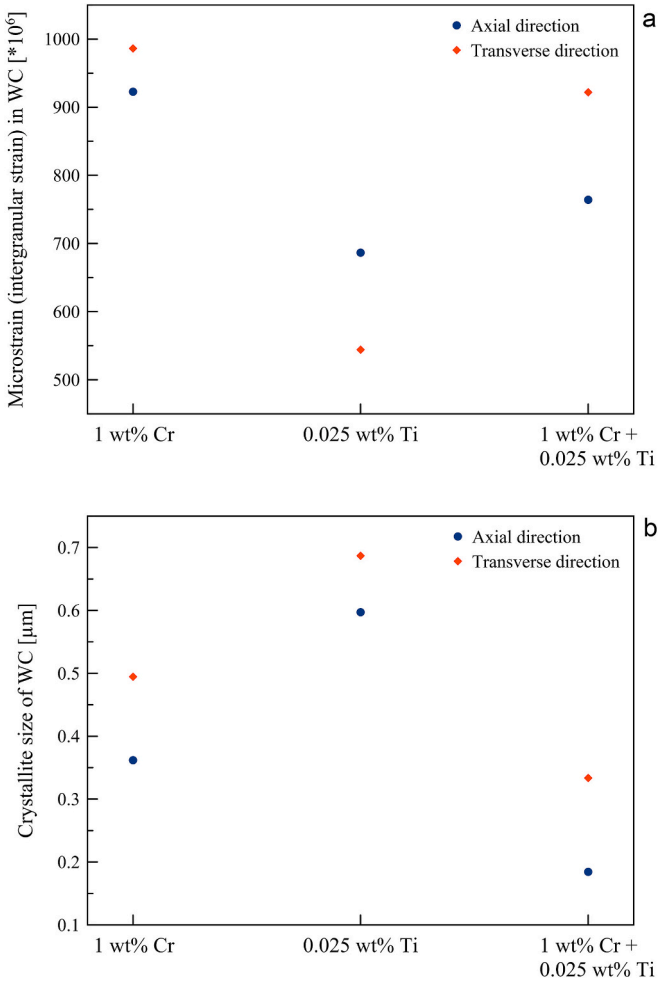

Fig. 10. Microstrain (a) and crystallite size (b) of WC phase in axial and transverse directions.

be seen for W and Co, where the calculations show higher Co and lower W values compared to the analysed composition. However, it is known that the M_7C_3 composition can vary within the C range and hence this may be a natural variation between the material and the compared graphite limit composition.

Segregation of Co and Ti to WC/WC grain boundaries has been reported before where the segregation is believed to have a strengthening effect [4,6]. The amount of segregation analysed in this study is higher than what has been reported earlier. The striped pattern of the segregant atoms has also been observed in the past and it is believed to be due to dislocations at the interface [6].

4.2. Estimation of residual stresses in binder

Residual stresses in the Co-rich binder phase are estimated using two approaches: (i) according to force balance by using the WC residual stress values and calculated volume fractions, i.e. in the absence of external load and assuming no macro-stress gradient, the sum of the volume-averaged stresses in WC and Co should be zero, and (ii) by using the lattice parameter of pure fcc-Co (3.5447 Å and Eqs. 1, 4 and 5, incorporating isotropic diffraction elastic constants $s_1 = -1.5166 \times 10^{-6}$ MPa^{-1} and $s_2/2 = 6.2559 \times 10^{-6}$ MPa^{-1} [19,22]. The estimations of the Co-rich binder residual stresses based on these two approaches are presented in Table 10. It should be noted that uncertainties exist in these estimates because, firstly, the overall macroscopic picture of residual stresses including the possible sub-surface gradients are not known and the assumption used means the stresses are balanced between phases, that is not true if there are macro-gradients where e.g. the compressive WC stresses in the center are balanced by tensile WC stresses at the surface; secondly, the lattice parameter of the binder phase may vary due to varying amounts of solutes in the binder phase. Nevertheless, using the force-balance estimation, we observe residual stress values similar to the previous findings [22]. The high tensile stresses in the binder phase suggest that it experiences severe plasticity during the cooling. One interesting finding is that, although the binder phase fraction and composition in Cr-doped and Cr and Ti co-doped systems are relatively identical, a trend opposite to that predicted by the force-balance assumption was observed. This suggests that estimating binder residual stresses is indeed a complex task and the calculation of residual stresses in the binder phase using force balance is an over-simplification. For a reliable quantitative view, one should account for the possible gradients within the components.

4.3. Evolution of residual stresses in WC

The results from this study show that the addition of Ti and Cr can significantly affect the residual stresses in the bulk WC-Co cemented carbides. Microstructural investigations as well as calculations reveal that the Cr and Ti addition alters the WC/WC grain and WC/Co interface boundary structure, the average WC grain size, and the Co-rich binder composition.

It has been reported that the magnitude of residual stresses in WC increases with reducing average WC grain size and increasing binder content [23]. As listed in Table 7, the EBSD findings show that average WC grain size varies within a narrow range from 0.377 µm (co-doped) to 0.418 µm (Cr-doped). Furthermore, the Cr-doped and co-doped materials have similar binder volume fractions as predicted by thermodynamic calculations. The observed presence of lowest WC residual stresses in the co-doped material can therefore not be explained by neither the average WC grain size nor the variation in binder volume fraction. We must therefore explore additional mechanisms contributing to the residual stresses observed in the three materials. It is known from a prior in-situ neutron diffraction study on the WC-Co (17 vol%) cemented carbide system that compressive residual stress starts to build-up in WC phase below 800 °C during cooling [24]. Various approaches, including Eshelby and Gurland models, have been used for the prediction of residual stresses in WC, where various parameters including in-situ binder yield strength, Young's modulus, and thermal expansion coefficients are considered [25,26]. The results from our study reveal that the binder composition varies due to the additions of Ti and/or Cr. Such variations in binder composition may not only affect the mechanical and thermal properties of binder phase but also influence the equilibrium conditions as depicted by equilibrium thermodynamics calculations (see Fig. 2). The phase diagrams show that the addition of 1 wt% Cr results in about 40 °C reduction in solidus temperature of binder phase and further reduction is predicted for co-doped system. Such difference in solidification temperature will surely influence the development of residual stresses, where a higher solidification may lead to more thermal mismatch considering the whole cooling cycle, while on the other hand the plastic accommodation of stresses is generally higher at high temperature. Regarding the calculated volumetric thermal

Table 10
Residual stresses in Co-rich binder estimated by using force balance and the lattice parameter of pure fcc—Co.

Cr additions (w%)	Ti additions (w%)	Force balance		fcc-Co lattice parameter	
		Axial (MPa)	Transverse (MPa)	Axial (MPa)	Transverse (MPa)
1	0	3365	3900	3857	3818
0	0.025	2278	3128	4556	4504
1	0.025	1997	1772	4342	4381

expansion coefficient, it was found that the mismatch between WC and the binder phase was predicted to largely vary with the relatively small changes in binder composition. These results are highly uncertain but would clearly affect the residual stresses after cooling.

The change of binder composition can also affect its strength by solute solution hardening and altering the stacking fault energy (SFE). At a constant binder volume fraction, mean free path, and thermal expansion coefficient, strengthening of the binder phase can lead to higher compressive residual stresses in the WC phase as Co-rich binder phase undergoes plastic deformation during the cooling after liquid phase sintering [26]. This is because a higher-strength binder phase would exert a greater load on the WC grains during contraction to maintain the volume consistency. It has been reported that Cr addition reduces the SFE of Co phase, which could facilitate the formation of Shockley partial dislocations and lead to more pronounced work hardening during cooling [27]. This increased work hardening may contribute to the higher WC residual stresses observed in the Cr-doped system. However, it is clear from the thermodynamic calculations that Cr is not the only element that changes, instead changes to Cr also affects, for example, W and C in solid solution.

As discussed in the APT section above there are changes to the interface segregations due to the doping, and the thermodynamics predictions at 1000 °C also show the formation of additional phases. Both interfacial layers and additional phases have the potential to contribute to the residual stress build-up. Whilst M_7C_3-type carbide formation is predicted in Cr-doped and co-doped systems, (Ti,W)C-type carbide is expected to be present in the Ti-doped material (see Tables 2 and 3).

As discussed above, the additional mechanisms behind residual stress development in doped WC-Co cemented carbides are unclear, but a number of possible mechanisms have been presented and we here propose further investigations on: i) how the interfacial layers and secondary carbide phases, thermal expansion mismatch and ii) SFE and mechanical properties of the binder phase affect residual stress development in cemented carbides. Furthermore, the contiguity of WC phase may also affect the residual stress development. It is believed that load sharing for WC is more effective with higher contiguity, similar to what is observed in a percolating dual-phase martensitic structure [28]. A higher load sharing capability should distribute macroscopic load more and results in less microscopic gradients build up, highlighting contiguity as an important parameter for future investigation.

5. Conclusions

(1) Co-doping of both Cr and Ti is advantageous for grain growth inhibition over just Cr- or Ti-doping.
(2) Small (5–10 nm) Cr-rich particles can form at the phase boundary region between WC and the binder phase. These particles are of the M_7C_3 phase which is a stable phase during sintering.
(3) The addition of Ti and Cr significantly affects the residual stresses in WC. Notably, the Cr and Ti co-doped material exhibits the lowest WC residual stresses despite similar WC average grain sizes and binder phase volume fractions compared to the Cr-doped material. This suggests that factors beyond grain size and Co-rich binder volume fraction such as binder SFE, thermal expansion coefficient and interface structure could be responsible for the observed differences in the WC residual stresses.
(4) In general, there are room for improvement of the assessment for the three systems in the used database for the thermodynamic calculations. As several phases needed to be removed during calculations and since phase solubility and stability not always agrees with experimental observations.

CRediT authorship contribution statement

J. Weidow: Writing – original draft, Supervision, Investigation, Conceptualization. **A.B. Yildiz:** Writing – original draft, Project administration, Investigation, Funding acquisition, Conceptualization. **G. Olsson:** Investigation. **V. Lilja:** Investigation. **S. Sten:** Investigation. **I. Borgh:** Writing – original draft, Supervision, Investigation, Conceptualization. **P. Hedström:** Writing – review & editing, Conceptualization. **M. Kritikos:** Conceptualization. **F. Lindberg:** Conceptualization. **E. Coronel:** Methodology. **J. Kelleher:** Investigation. **D. Mayweg:** Supervision. **M. Thuvander:** Supervision. **S. Norgren:** Conceptualization.

Declaration of competing interest

The authors declare that they have no known competing financial interests or personal relationships that could have appeared to influence the work reported in this paper.

Data availability

No data was used for the research described in the article.

Acknowledgements

The allocation of beamtime through The ISIS Industrial Collaborative R&D programme is gratefully acknowledged (Reference number: ICRD0077). This research was funded by the Swedish Agency for Innovation Systems, VINNOVA, within the programme “Industrial utilization of neutron and synchrotron light-based technologies in large-scale research infrastructure” (Reference number: 2021-03839).

References

[1] K. Hayashi, Y. Fuke, H. Suzuki, Effects of addition carbides on the grain size of WC-Co alloy, J. Jpn. Soc. Powder Metall. 19 (1972) 67–71.
[2] T. Yamamoto, Y. Ikuhara, T. Watanabe, T. Sakuma, Y. Taniuchi, K. Okada, T. Tanase, High resolution microscopy study in Cr_3C_2-doped WC−Co, J. Mater. Sci. 36 (2001) 3885–3890.
[3] A. Delanoë, M. Bacia, E. Pauty, S. Lay, C.H. Allibert, Cr-rich layer at the WC/Co interface in Cr-doped WC-Co cermets: segregation or metastable carbide? J. Cryst. Growth 270 (2004) 219–227.
[4] M. Christensen, G. Wahnström, Strength and reinforcement of interfaces in cemented carbides, Int. J. Refract. Met. Hard Mater. 24 (2006) 80–88.
[5] J. Weidow, H.-O. Andrén, Grain and phase boundary segregation in WC-Co with small V, Cr or Mn additions, Acta Mater 58 (2010) 3888–3894.
[6] J. Weidow, H.-O. Andrén, Grain and phase boundary segregation in WC-Co with TiC, ZrC, NbC or TaC additions, Int. J. Refract. Met. Hard Mater. 29 (2011) 38–43.
[7] D. Mari, B. Clausen, M.A.M. Bourke, K. Buss, Measurement of residual thermal stress in WC-Co by neutron diffraction, Int. J. Refract. Met. Hard Mater. 27 (2009) 282–287.
[8] M.T. Hutchings, A.D. Krawitz (Eds.), Measurement of Residual and Applied Stress Using Neutron Diffraction 216, Springer Science & Business Media, 1992.
[9] G.S. Schajer (Ed.), Practical Residual Stress Measurement Methods, John Wiley & Sons, 2013.
[10] M.A. Yousfi, A. Nordgren, S. Norgren, J. Weidow, H.-O. Andrén, L.K.L. Falk, Creep of un-doped and Cr-doped WC-Co at high temperature and high load, Int. J. Refract. Met. Hard Mater. 117 (2023) 106417.
[11] J.O. Andersson, T. Helander, L. Höglund, P.F. Shi, B. Sundman, Thermo-Calc and DICTRA, computational tools for materials science, Calphad 26 (2002) 273–312.
[12] H.-O. Andrén, Microstructures of cemented carbides, Mater. Des. 22 (2001) 491–498.
[13] N. Heshmati, M. Hoseini-Athar, E. Olsson, A. Borgenstam, H. Sieurin, J. Larsson, T. L. Lee, P. Hedström, On the overlooked role of microstructure to explain post-punching fatigue performance of advanced high-strength steel, J. Mater. Res. Technol. (2024).
[14] Scatterin SaaS data analysis software. https://saas.scatterin.com/, 2024.
[15] H.M. Rietveld, A profile refinement method for nuclear and magnetic structures, J. Appl. Cryst. 2 (1969) 65–71.
[16] R.J. Hill, C.J. Howard, Quantitative phase analysis from neutron powder diffraction data using the Rietveld method, J. Appl. Cryst. 20 (1987) 467–474.
[17] K.D. Litasov, A. Shatskiy, Y. Fei, A. Suzuki, E. Ohtani, K. Funakoshi, Pressure-volume-temperature equation of state of tungsten carbide at 32 GPa and 1673 K, J. Appl. Phys. 108 (2010) 053513.
[18] J.W. Paggett, A.D. Krawitz, E.F. Drake, M.A.M. Bourke, V. Livescu, B. Claussen, D. W. Brown, In situ loading response of WC–Ni: origins of toughness, Int. J. Refract. Met. Hard Mater. 24 (2006) 122–128.
[19] R.N. Abdullaev, Density and thermal expansion of high purity cobalt over the temperature range from 140 K to 2073 K, Metal. Mater. Trans. A 52A (5449) (2021) 5456.
[20] M. Nuding, M. Ellner, Influence of the isotypical A9, A10 and B11 solvents on the partial atomic volume of tin, J. Alloys Compd. 252 (1997) 184–191.

[21] M. Thuvander, J. Weidow, J. Angseryd, L.K.L. Falk, F. Liu, M. Sonestedt, K. Stiller, H.-O. Andrén, Quantitative atom probe analysis of carbides, Ultramicroscopy 111 (2011) 604–608.
[22] J.W. Paggett, Neutron Diffraction Study of Load Response and Residual Stresses in WC-(Ni/Co) Composites, University of Missouri-Columbia, 2005.
[23] D.L. Coats, A.D. Krawitz, Effect of particle size on thermal residual stress in WC–Co composites, Mater. Sci. Eng. A 359 (2003) 338–342.
[24] D. Mari, B. Clausen, M.A.M. Bourke, Buss K measurement of residual thermal stress in WC–Co by neutron diffraction, Int. J. Refract. Met. Hard Mater. 27 (2009) 282–287.
[25] A. Krawitz, E. Drake, Residual stresses in cemented carbides—an overview, Int. J. Refract. Met. Hard Mater. 49 (2005) 27–35.
[26] L. Degeneve, D. Mari, P.V.S. Machado, E. Jimenez-Piqué, FEM of stress partition during compression of WC-10 wt.% Co with realistic 3D morphology, Int. J. Refract. Met. Hard Mater. 111 (2023) 106083.
[27] L.Y. Tian, R. Lizárraga, H. Larsson, E. Holmström, L. Vitos, A first principles study of the stacking fault energies for fcc Co-based binary alloys, Acta Mater. 136 (2017) 215–223.
[28] Y. Tian, S. Lin, J.P. Ko, U. Lienert, A. Borgenstam, P. Hedström, Micromechanics and microstructure evolution during in situ uniaxial tensile loading of TRIP-assisted duplex stainless steels, Mater. Sci. Eng. A 734 (2018) 281–290.